Structure Elucidation |*Hot Paper*|

Biuret—A Crucial Reaction Intermediate for Understanding Urea Pyrolysis To Form Carbon Nitrides: Crystal-Structure Elucidation and In Situ Diffractometric, Vibrational and Thermal Characterisation

Peter Gross and Henning A. Höppe*[a]

Abstract: The crystal structure of biuret was elucidated by means of XRD analysis of single crystals grown through slow evaporation from a solution in ethanol. It crystallises in its own structure type in space group *C*2/*c* ($a = 15.4135(8)$ Å, $b = 6.6042(3)$ Å, $c = 9.3055(4)$ Å, $Z = 8$). Biuret decomposition was studied in situ by means of temperature-programmed powder XRD and FTIR spectroscopy, to identify a co-crystalline biuret–cyanuric acid phase as a previously unrecognised reaction intermediate. Extensive thermogravimetric studies of varying crucible geometry, heating rate and initial sample mass reveal that the concentration of reactive gases at the interface to the condensed sample residues is a crucial parameter for the prevailing decomposition pathway. Taking these findings into consideration, a study on the optimisation of carbon nitride synthesis from urea on the gram scale, with standard solid-state laboratory techniques, is presented. Finally, a serendipitously encountered self-coating of the crucible inner walls by graphite during repeated synthetic cycles, which prove to be highly beneficial for the obtained yields, is reported.

Introduction

Despite its simple constitution, urea ($NH_2C(O)NH_2$) has kept scientists of various disciplines busy over the last four centuries.[1] Its exploration has triggered some of the most pivotal discussions in the history of science, including Prout's hypothesis,[2] the Vitalism debate[3] or the theory of metabolic cycles,[4] many of which revolve around the nature of urea formation/degradation. In particular, the presumably simple, dry and uncatalysed pyrolysis of urea "largely remains a mystery and a challenge to investigators",[5] to date. In addition to these persisting fundamental questions of molecular chemistry, renewed exploration of this topic in recent years has been driven by engineers and catalysis chemists, on one hand,[6–9] due to the increasing use of urea as a reductant for the selective catalytic reduction (SCR) of nitrous oxides in the after-treatment of exhaust gases from diesel engines,[10] and by materials scientists, on the other hand,[11] due to the recent discovery[12] of urea as precursor to carbon nitride materials.[13] As often happens, one man's meat is another man's poison: although solid by-products of urea pyrolysis are one of many challenges for the implementation of mobile SCR technologies,[14,15] the sum of which were a partial motivation for what, in 2015, came to light as the so-called diesel emissions scandals,[16] carbon nitrides are heavily researched as potential superhard materials,[17] novel semiconductors,[18] luminescent materials,[19,20] catalysts and catalyst substrates,[21] materials for photocatalytic water splitting[22] and because of fundamental questions of structural chemistry.[23–25] Therefore, a better understanding of urea pyrolysis remains a crucial challenge for scientists from a huge variety of disciplines.

To shine some light onto urea pyrolysis, many thermogravimetric and calorimetric studies have been conducted, often in combination with the analysis of evolved gases and/or pyrolysis residues by means of vibrational spectroscopy, mass spectrometry or chromatography, as well as thermochemical modelling of the decomposition reaction.[7,26–40] Several studies explicitly reveal the distinct influence of pyrolysis parameters, such as heating rate, initial sample mass and crucible shape on decomposition temperature, total mass loss and pyrolysis residues formed.[5,9,41,42] This might be traced back to the complex mix of different reaction products and intermediates during urea pyrolysis (the specific composition is determined by the exact pyrolysis parameters), many of which can further react with each other to form different intermediates. Among them, ammonia, cyanic acid, carbon dioxide, water, biuret

[a] *P. Gross, Prof. Dr. H. A. Höppe*
Lehrstuhl für Festkörperchemie, Universität Augsburg
Universitätsstr. 1, 86159 Augsburg (Germany)
E-mail: henning@ak-hoeppe.de
Homepage: https://www.ak-hoeppe.de

Supporting information and the ORCID identification number(s) for the author(s) of this article can be found under: https://doi.org/10.1002/chem.202001396. It contains further figures illustrating powder diffraction patterns, XPS spectra, as well as FTIR spectra and tables comparing vibrational frequencies.

($H_2NC(O)NHC(O)NH_2$), triuret ($H_2N(C(O)NH)_2C(O)NH_2$), cyanuric acid ($H_3[C_3N_3O_3]$), ammelide ($H_2[C_3N_3O_2(NH_2)]$), ammeline ($H[C_3N_3O(NH_2)_2]$), melamine ($[C_3N_3(NH_2)_3]$), melam ($[C_3N_3(NH_2)_2]NH[C_3N_3(NH_2)_2]$), melem ($[C_6N_7(NH_2)_3]$) and melon ($[C_6N_7(NH_2)(NH)]_n$, the last of which is often somewhat misnamed graphitic carbon nitride (g-C_3N_4) throughout the literature,[24] have been found. All of them have been known since the pioneering works of Berzelius,[43] Liebig[44] and Wöhler,[45] and all contribute to the complexity of this pyrolysis with their individual kinetics of formation and decomposition in often overlapping temperature regimes. The thermal decomposition path of urea, as generally established in literature, can be broken down into the simplified reaction steps given in Equations (1)–(15):

$$T \geq 133\,^{\circ}\mathrm{C} \qquad \mathrm{urea}_m \rightleftharpoons \mathrm{NH_4(OCN)}_m \quad \mathrm{NH_4(OCN)}_m \rightarrow \mathrm{NH_{3(g)}} + \mathrm{HOCN_{(g)}} \tag{1}$$

$$T \geq 150\,^{\circ}\mathrm{C} \qquad \mathrm{urea}_m \xrightarrow{+\mathrm{HNCO}} \mathrm{biuret} \tag{2}$$

$$T \geq 160\,^{\circ}\mathrm{C} \qquad \mathrm{biuret} \rightarrow \mathrm{urea}_m + \mathrm{HOCN_{(g)}} \tag{3}$$

$$T \geq 160\,^{\circ}\mathrm{C} \qquad 3\,\mathrm{HNCO} \rightarrow \text{cyanuric acid} \tag{4}$$

$$T \geq 160\,^{\circ}\mathrm{C} \qquad \mathrm{biuret} \xrightarrow{+\mathrm{HNCO}} \mathrm{triuret} \tag{5}$$

$$T \geq 160\,^{\circ}\mathrm{C} \qquad \mathrm{biuret} \xrightarrow[-\mathrm{NH_3}]{+\mathrm{HNCO}} \text{cyanuric acid} \tag{6}$$

$$T \geq 160\,^{\circ}\mathrm{C} \qquad \mathrm{urea} \xrightarrow[-\mathrm{H_2O}]{+2\,\mathrm{HNCO}} \mathrm{ammelide} \tag{7}$$

$$T \geq 190\,^{\circ}\mathrm{C} \qquad \mathrm{triuret} \xrightarrow[-\mathrm{NH_3}]{} \text{cyanuric acid} \tag{8}$$

$$T \geq 190\,^{\circ}\mathrm{C} \qquad \mathrm{biuret} \xrightarrow[-\mathrm{H_2O}]{+\mathrm{HNCO}} \mathrm{ammelide} \tag{9}$$

$$T \geq 250\,^{\circ}\mathrm{C} \qquad \text{cyanuric acid} \rightarrow 3\,\mathrm{HNCO} \tag{10}$$

$$T \geq 250\,^{\circ}\mathrm{C} \qquad \mathrm{ammelide} \xrightarrow[-\mathrm{H_2O}]{+\mathrm{NH_3}} \mathrm{ammeline} \tag{11}$$

$$T \geq 250\,^{\circ}\mathrm{C} \qquad \mathrm{ammeline} \xrightarrow[-\mathrm{H_2O}]{+\mathrm{NH_3}} \mathrm{melamine} \tag{12}$$

$$T \geq 350\,^{\circ}\mathrm{C} \qquad 2\,\mathrm{melamine} \xrightarrow[-\mathrm{NH_3}]{} \mathrm{melam} \tag{13}$$

$$T \geq 350\,^{\circ}\mathrm{C} \qquad 2\,\mathrm{melam} \xrightarrow[-\mathrm{NH_3}]{} \mathrm{melem} \tag{14}$$

$$T \geq 350\,^{\circ}\mathrm{C} \qquad n\,\mathrm{melem} \xrightarrow[-n\,\mathrm{NH_3}]{} \mathrm{melon} \tag{15}$$

It should be noted that these reaction steps, as well as the temperature ranges reported throughout the literature, might vary, depending on the theoretical and experimental methods and parameters chosen. Only the first two steps, that is, the melting and evaporation of urea [Eq. (1)], as well as the subsequent formation of biuret [Eq. (2)], are agreed upon in all studies, with a few notable exceptions.[39] The challenge of understanding the reaction pathway of urea decomposition might therefore be simplified, to a certain degree, to the problem of biuret decomposition.

However, the variety of reported reaction pathways is also more deeply routed in the ambiguity inherent to thermal analysis, and as Kohlmann recently emphasised: "The lack of specificity of thermal signals is a disadvantage, which usually asks for complementary structural in situ methods, like diffraction or spectroscopy on the solids".[46] Astonishingly, to date, neither spectroscopic nor diffractometric characterisation techniques have been used to study the pyrolysis of urea and its decomposition products in situ. In particular, the absence of diffraction studies is striking, especially with regard to the crystallographic breakthroughs historically achieved with urea and its decomposition products.[47] One reason for the lack of in situ probing of urea, although this does not hold for its decomposition products, might be the complications linked with its melting and evaporation,[48] which we have also encountered during our preliminary studies and that have prevented us from conducting in situ powder XRD and FTIR measurements of urea. Furthermore, to the best of our knowledge, no study on the crystal structure of water-free biuret (the simplest urea decomposition product already described by Wiedemann over 170 years ago[49]) has been published, although the crystal structures of biuret hydrate[50,51] and several other crystal structures containing biuret molecules[52–57] have been elucidated. We therefore decided to contribute our attempt to solve this ongoing interdisciplinary chemical conundrum by reporting on our structural and vibrational characterisation of biuret, as well as in situ powder XRD and FTIR measurements during its thermal decomposition. Furthermore, we present a comprehensive thermogravimetric study on biuret, varying heating rate, initial mass, crucible form and atmosphere over a large parameter range. Finally, we put all lessons learned into use by optimising the yield of a gram-scale synthesis of melon directly from urea.

Results

Crystal structure of biuret

Biuret crystallises in a new structure type in the monoclinic space group *C*2/*c* (no. 15) with eight molecules per unit cell, as depicted in Figure 1. Relevant parameters of the crystal-structure refinement are given in Table 1. All atoms are situated on general positions. The biuret moiety shows that the *trans* configuration exclusively is almost perfectly flat (largest torsion angle: 3°) and oriented either parallel to (19 7 $\overline{11}$) or to (19 $\bar{7}$ $\overline{11}$). The averaged interatomic distances for C–O (1.24 Å), C–Ni (1.38 Å, imide N) and C–Na (1.32 Å, amide N) correspond very well to the values found in other biuret-containing crystal structures and to the sum of the ionic radii (Table 2).[58] The molecule features one intramolecular hydrogen bond between one carbonyl and one amide group (O–H distance: 1.92 Å), as well as two intermolecular hydrogen bonds between amide and carbonyl groups towards each of the two adjacent, coplanar biuret molecules, forming two sets of skew ribbons ubiquitous in the crystal chemistry of ureas (Figure 1b).[51,59–62] The ribbons within a set are stacked antiparallel offset with a inter-ribbon distance of about 3.3 Å, roughly corresponding to the sum of the van der Waals radii of N/O and C. One set of these ribbons traverses the unit cell roughly parallel to [10 $\bar{5}$ $\bar{1}$], the other parallel to [14 11 $\bar{2}$], with a dihedral angle of about 53.5° between the two ribbon planes, resulting in a criss-cross pattern with rhombical channels along (11 0 6) (Figure 1c). The di-

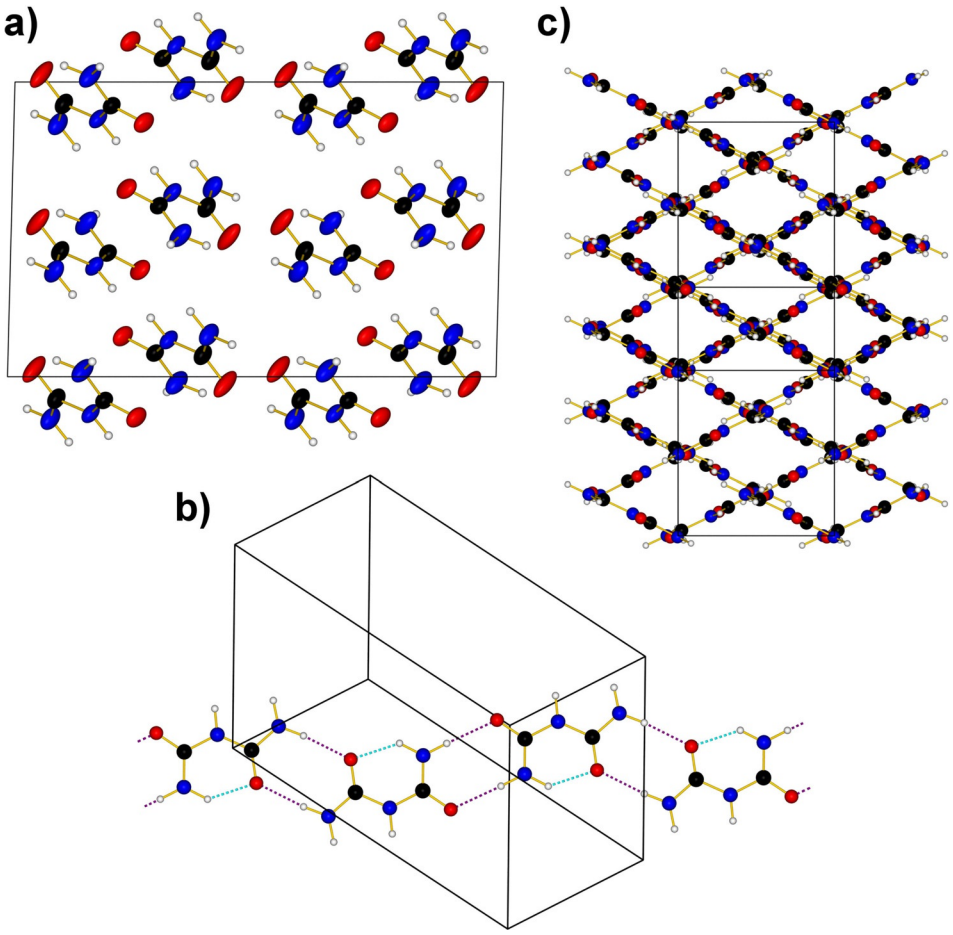

Figure 1. a) The unit cell of biuret viewed along [0 1 0] (H atoms in white, C atoms in black, N atoms in blue, O atoms in red and covalent bonds as yellow sticks; ellipsoids correspond to 50% probability). b) Ribbons formed through hydrogen bonds between coplanar biuret molecules viewed along [19 7 $\overline{11}$] (intramolecular hydrogen bonds as light-blue broken lines, intermolecular hydrogen bonds as violet broken lines). c) Criss-cross pattern formed by hydrogen bonds between skew ribbons viewed along [11 0 6].

Table 1. Crystal data and structure refinement of biuret.

Parameter	Biuret
formula	$C_2H_5N_3O_2$
M_r [g mol^{-1}]	103.09
crystal size [mm^3]	0.50×0.02×0.01
crystal system	monoclinic
space group	*C*2/*c*
a [Å]	15.4135(8)
b [Å]	6.6042(3)
c [Å]	9.3055(4)
β [°]	91.463(3)
V [Å^3]	946.93(8)
Z	8
D_{calcd} [g cm^{-1}]	1.446
$\mu(Mo_{K\alpha})$ [cm^{-1}]	0.143
F (000) [e]	432
hkl range	18, 7, 11
$[(\sin\theta)/\lambda]_{max}$ [Å^3]	0.59
measured reflns	24 899
unique reflns	828
R_{int}/R_{sigma}	0.099/0.024
no. refined parameters	79
$R_1(F)/wR_2(F^2)$ (all reflns)	0.068/0.095
GoF (F^2)	1.06
$\Delta\rho_{fin}$ (max/min) [e Å^{-3}]	0.14/−0.17

Table 2. Selected interatomic distances [Å] and angles [°] for biuret and biuret hydrate,[51] as well as the sum of the ionic radii, $\Sigma_i r_i$.[58]

	Biuret	Biuret hydrate[51]	$\Sigma_i r_i$
C–N_a[a]	1.32–1.33	1.33–1.36	1.38
C–N_i[a]	1.38	1.39–1.40	1.38
C–O	1.23–1.24	1.25–1.26	1.26
N-C-N	114–119	124	
C-N-C	128	117	
N_a-C-O[a]	123–124	121–125	
N_i-C-O[a]	118–122	117–125	

[a] Atom labelling: i: atom belonging to the imide group; a: atom belonging to the amide group.

ameter of the resulting channel corresponds to the inter-ribbon distance, so the crystal structure can be regarded as close packed. This packing can be further rationalised by regarding dimers of stacked biuret molecules belonging to two neighbouring parallel ribbons (Figure 2a). These dimers do not reflect the closest intermolecular distances between biuret molecules, but facilitate an understanding of the packing motif because they feature nearly equal distances between the two

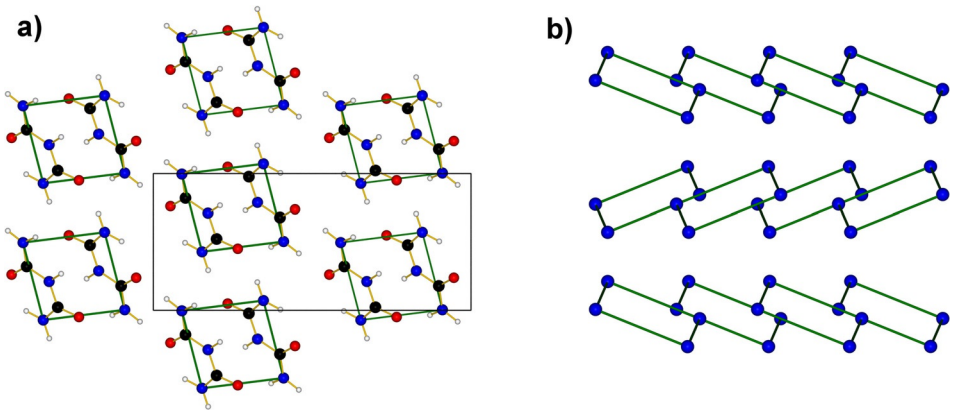

Figure 2. a) Hexagonal close-packed layer of biuret dimers viewed along [0 0 1] (green rhombi outline the dimers as a line to guide the eye). b) AB stacking of layers to form hexagonal closest packing (for the sake of clarity, only outlines and corners of the rhombi are shown).

amidic nitrogen atoms within a molecule and between molecules, forming rhombi. These rhombi are arranged in hexagonal packing in the (1 1 0) plane (Figure 2a), reflecting the rhomboidal channels described before. The hexagonal layers are stacked in an AB sequence along [0 0 1], resulting in hexagonal closest packing of dimers (Figure 2b).

Characterisation of biuret and cyanuric acid at room temperature

Phase purity of the employed biuret and cyanuric acid samples was ensured by means of powder XRD (Figure S1 in the Supporting Information). The infrared spectra of biuret and cyanuric acid were recorded between 4000 and 400 cm^{-1} through attenuated total reflectance (ATR; Figure S2 in the Supporting Information). Both agree very well with the spectra found in literature (Table S1 in the Supporting Information). Although the temperature-programmed (TP) spectra were recorded by DRIFTS, the room-temperature ATR spectra were used as a reference for their interpretation, as well as for mode assignment due to their better signal-to-noise ratio.

In situ XRD and FTIR spectrometry

Because our crystal-structure determination of biuret allowed us to unambiguously assign its phase to a powder XRD pattern, we could study its decomposition in situ by means of temperature-programmed powder XRD (TP-XRD). Figure 3

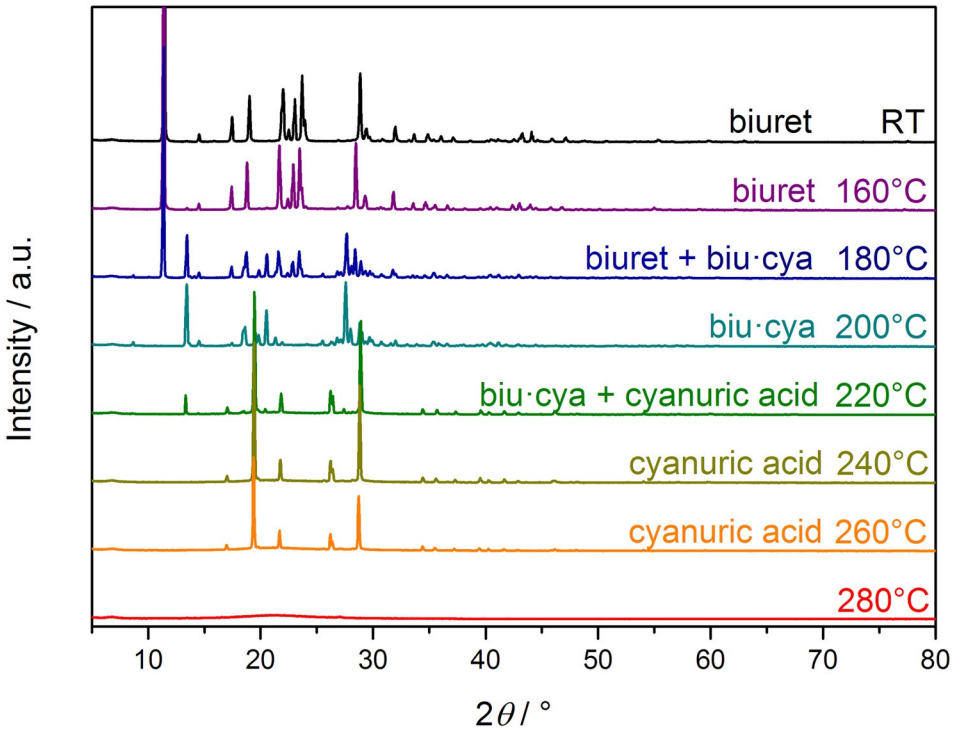

Figure 3. TP-XRD results and phase assignment during biuret decomposition between room temperature and 280 °C (biu·cya denotes the 1:1 biuret/cyanuric acid co-crystalline phase).

shows selected TP-XRD patterns collected during the decomposition of biuret. From room temperature to about 160 °C, biuret is the only phase observed (cf. Figure S3 in the Supporting Information). Between 160 and 180 °C, a co-crystalline phase of biuret and cyanuric acid in a ratio of 1:1 appears (cf. Figure S4 in the Supporting Information), the crystal structure of which was already elucidated for single crystals obtained through solution-growth experiments.[53] At 200 °C, the transformation process to this phase is complete and already a few small reflections appear that can be attributed to cyanuric acid. Further heating to 240 °C leads to the disappearance of all reflections linked to the co-crystalline phase and only cyanuric acid remains as a phase-pure powder (cf. Figure S5 in the Supporting Information). Further heating leads to diminished intensities of all reflections, until they disappear completely between 260 and 280 °C. Although several of the proposed aminated, condensed decomposition products of biuret [Eqs. (8) and (10)–(14)], such as melem,[63,64] melam,[65,66] melamine[67] or co-crystals containing the last two,[63,66,68] are known to crystallise quite well, no traces of them could be detected by means of TP-XRD.

These findings were confirmed by means of TP-DRIFTS to rule out the presence of such aminated, condensed species as amorphous side phases in larger quantities. As observed in Figure 4, the spectra suggest a continuous transition from a spectrum identical to that of biuret (shown as a black curve at the top) below 160 °C, via one characteristic for the 1:1 biuret/cyanuric acid co-crystalline phase (inserted as a black curve between the spectra at 180 and 200 °C) at about 200 °C, to a spectrum nearly identical to that of cyanuric acid (shown as a black curve at the bottom) above 280 °C. The broad and intense band at 860 cm^{-1} can be seen as an indicator for the formation and decomposition of the co-crystalline phase, since it is neither present in the biuret nor cyanuric acid spectra, and is most probably tied to a N–H bending vibration of a group involved in hydrogen bonding between two different molecular species. Again, no traces of aminated, condensed species could be identified within our means, especially no discrete, sharp absorptions at about 3500 cm^{-1} characteristic for NH_2 groups (as would be present in melamine, melem, melam or melon).[63,66,68]

Thermogravimetric analysis (TGA) of biuret

To understand why our in situ studies did not reveal any indication of amination of urea derivatives, although these are clearly shown to occur through a range of other techniques,[5–7,9,29,41] we decided to explore the specific pyrolysis parameters under which such species occurred through TGA, in terms of crucible shape, heating rate, initial sample mass and atmosphere. Therefore, four series of TGA experiments were conducted on biuret: series A, varying crucible shape (plate, open cylinder, cylinder closed with a lid; Figure 5a); series B, varying heating rate (0.3–50 K min^{-1}; Figure 5b); series C, varying employed sample mass (1–81 mg; Figure 5c) and series D, varying flushing gas flow rate (10–150 mL min^{-1}, flushing gas: N_2). Although variation of the last of these produced virtually identical TGA curves for the whole series, and is therefore not discussed, variation of the parameters in series A, B and C reveals a massive impact on temperatures and mass

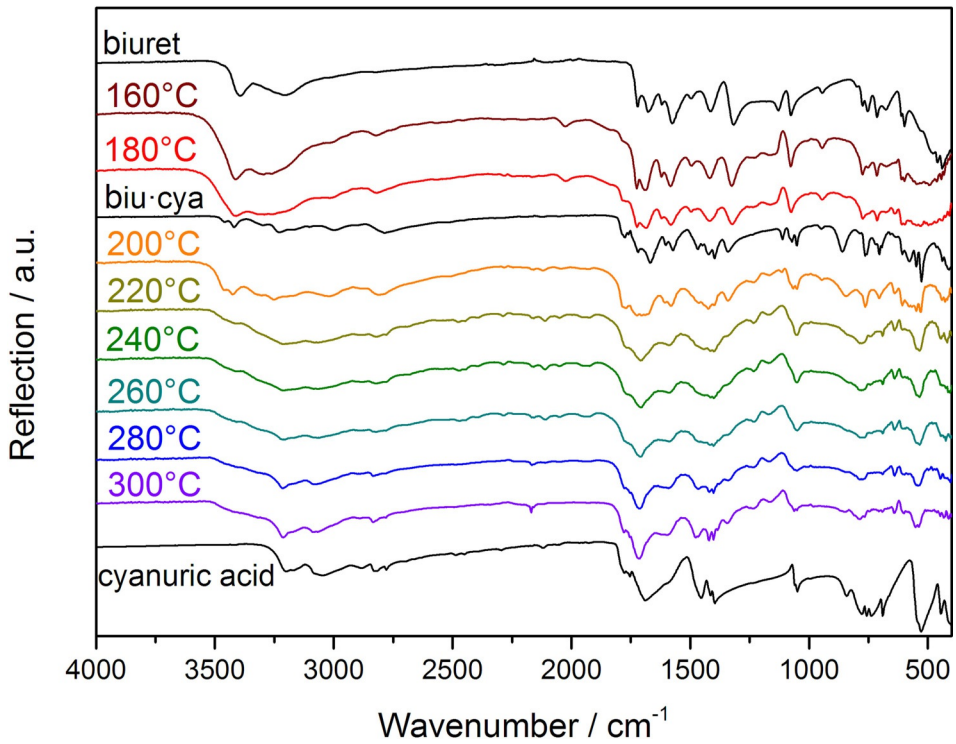

Figure 4. TP FTIR spectroscopy during biuret decomposition between 160 and 300 °C, as well as reference spectra of phase-pure samples of biuret, 1:1 biu·cya co-crystalline phase and cyanuric acid (black curves inserted in between).

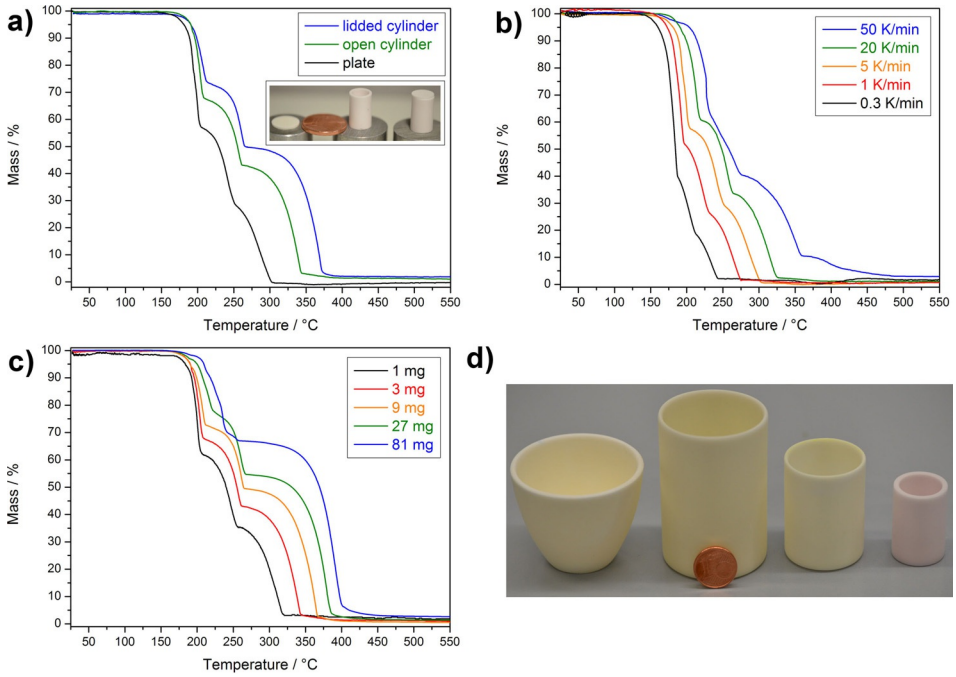

Figure 5. a) Thermograms of biuret measured with different crucible shapes (the inset shows the employed crucibles together with a €1 cent coin for scale). b) Thermograms of biuret measured at different heating rates (0.3–50 K min^{-1}). c) Thermograms of biuret measured with different initial sample masses (1–81 mg). d) Photograph of the different crucibles employed for melon synthesis with a €1 cent coin for scale.

losses observed for the respective decomposition steps, as well as masses of pyrolysis residues remaining at 550 °C. Parameters of the experimental setup, together with crucial characteristics of the obtained thermograms, are compiled in Table 3. Despite large quantitative differences, the general shape of the thermogravimetric curves during most experiments throughout the four series remains similar and can be exemplarily discussed for a typical thermogram (green curve in Figure 5a; red curve in Figure 5c), as summarised in the first entry for series A and third entry for series B in Table 3 (gas flow rate of 70 mL min^{-1}, open cylindrical crucible, initial sample mass $m_0 = 3$ mg, heating rate $\Delta T = 5$ K min^{-1}). Four major decomposition ranges can be observed: the first between 165 and 210 °C, accounting for about 33.3% mass loss; the second between 210 and 265 °C, accounting for about 25% mass loss; the third between 265 and 345 °C, accounting for about 40% mass loss; and the last between 345 and 400 °C, accounting for about 1.7% mass loss. The first decomposition range is further divided into two sub-steps (7.7 and 25.6% mass loss, respectively) visible as a shoulder at about 193 °C. The position of the shoulder during the first decomposition range coincides reasonably well with the melting point ($T_m = 193$ °C) of biuret.[28] We therefore attribute the first sub-step to partial decomposition of biuret in the solid state to cyanuric acid, until the melting point is reached, followed by the second sub-step of enhanced decomposition of biuret in the

Table 3. Parameters of the experimental setup (crucible shape, heating rate ΔT, employed sample mass m_0) and selected characteristics of the obtained thermograms (temperature range T and mass loss Δm of the first, second and third decomposition steps, as well as the relative mass of the pyrolysis residue m_{pr}) for series A–C (flush gas flow rate kept constant at 70 mL min^{-1}).

Series	Crucible	ΔT [K min^{-1}]	m_0 [mg]	T_{1st} [°C]	Δm_{1st} [%]	T_{2nd} [°C]	Δm_{2nd} [%]	T_{3rd} [°C]	Δm_{3rd} [%]	m_{pr} [%]
A	plate	5	2.9	155–205	42.2	205–255	29.5	255–305	28.0	0
A	cylinder	5	3.1	165–210	32.3	210–262	24.7	262–345	40.0	1.0
A	cylinder with lid	5	3.0	170–215	25.4	215–267	23.7	267–375	46.5	2.8
B	plate	0.3	2.9	135–187	59.5	187–213	21.8	213–243	16.2	0
B	plate	1	3.0	140–198	49.1	198–232	25.3	232–275	24.8	0
B	plate	5	2.9	155–205	42.2	205–255	29.5	255–305	28.0	1.0
B	plate	20	3.0	160–223	39.5	223–267	27.1	267–328	30.9	1.2
B	plate	50	3.0	150-230	34.6	230-275	24.9	275-360	30.1	2.4
C	cylinder	5	1.0	165–207	35.8	207–257	27.3	260–320	31.9	0
C	cylinder	5	3.1	165–210	32.3	210–262	24.7	262–345	40.0	1.0
C	cylinder	5	8.9	165–212	26.8	212–265	23.0	265–367	46.8	1.0
C	cylinder	5	27.1	165–222	21.7	222–269	23.3	269–390	51.3	1.3
C	cylinder	5	80.8	165–233	20.3	233-257	12.3	260–400	60.4	2.6

melt. The first and second decomposition ranges of biuret together can be, for the most part, assigned to the formation of cyanuric acid, according to Equations (3), (2) and (6). Our in situ diffractometric and spectroscopic measurements could, for the first time, unambiguously explain why the degradation of biuret to cyanuric acid occurs through two energetically well-separated decomposition steps, as the 1:1 co-crystalline phase of biuret and cyanuric acid has been identified as a clearly thermodynamically favoured reaction intermediate. Because the calculated overall mass loss for the complete reaction towards cyanuric acid totals 16.5%, the measured value of 56% indicates that large amounts of urea, biuret and/or HNCO + NH_3 directly evaporate without further reaction with the condensed species, according to Equations (3)–(6); we note that it is long known that HNCO is highly volatile and its reactivity strongly depends on concentration and temperature.[69,70] Although urea derivatives with a higher degree of amination and/or condensation (i.e., ammelide, ammeline, melamine, melam, melem and melon) could neither be directly seen by TP-XRD and TP-DRIFTS, nor as a single, separated step in the thermograms, the occasional presence of a fourth decomposition range, in which the gradual degradation of melamine via melam and melam towards melon occurred,[68] as well as the presence of high-temperature pyrolysis residues (melon and related carbon nitrides) indirectly indicated their occurrence during the first three decomposition ranges.

Changing the openness of the crucible towards the surrounding flushing gas by changing it from a plate to an open cylinder and then to a cylinder closed with a lid within series A shifts the temperature range of the first major decomposition step to higher temperatures accompanied by lower mass losses. These changes can be rationalised as less gas exchange between the atmosphere directly above the sample and the flushing gas stream, so that both retain more gaseous urea/HNCO [Eqs. (1), (3)–(6) and (9)] and NH_3 [Eqs. (10) and (11)] directly at the solid/liquid–gas interface to further react to form condensed products, resulting in smaller mass losses and a shift of the chemical equilibrium towards the educt side, requiring higher temperatures for decomposition to occur. Consequently, the third decomposition range shows the same trend with regard to temperature and the reverse trend regarding mass loss because monomerisation and evaporation of cyanuric acid, according to Equation (9), is prone to the same effects, whereas larger amounts of cyanuric acid form in the first place to allow for larger mass losses through evaporation later. The fourth decomposition range is absent for the plate-shaped crucible, possibly because not enough aminated species have been formed for detection, and it is blended into the third decomposition range for the crucible closed with a lid, since the decomposition of cyanuric acid is shifted to sufficiently to high temperatures to occur in parallel to that of melamine. The residual masses at 550 °C follow the same pattern, indicating that an open crucible shape results in the formation of a low amount of carbon nitrides because a lesser degree of evolved NH_3 remains available for amination reactions at the solid/liquid–gas interface at lower temperatures.

Varying the heating rate ΔT within series B of our TGA experiments corroborates these findings. The temperature range for the first major decomposition step shifts gradually to higher temperatures with increasing heating rates, whereas the corresponding mass loss drastically decreases from 59.5 to 34.6%. Although the former could, in part, also be attributed to simple thermal inertia of the experimental setup, the latter is a clear sign of a higher reaction rate of urea/HNCO and NH_3 with the solid/liquid species in the crucible, which is caused by a higher concentration of reactive gases directly at the solid/liquid–gas interface. The second major decomposition range shifts to higher temperatures, with corresponding mass losses increasing up to $\Delta T = 5\ K\,min^{-1}$ and finally decreasing again for higher heating rates. Although the shift of the temperature range can be attributed to the same reasons as those in the first decomposition range, decreasing mass losses for very high heating rates indicate a considerable amount of amination during the first two decomposition ranges, as well as a lower relative amount of biuret left to decompose during the second step if decomposition were severe enough during the first step. The third decomposition range shifts to higher temperatures for the same reasons, while the linked mass loss increases. The residual mass left at 550 °C increases from below the detection limit for $\Delta T = 0.3\ K\,min^{-1}$ to 2.4% for $\Delta T = 50\ K\,min^{-1}$, which also supports this interpretation.

The thermograms of series C, which are measured by employing varying initial sample masses m_0 within crucibles of the same size and shape, overall further corroborate our working hypothesis of reactive gas concentration at the solid/liquid–gas interface being a crucial parameter for the reaction pathway during decomposition of biuret and its degradation products. Although the onset of the first decomposition range is consistently at about 165 °C, its completion shifts to higher temperatures with increasing initial masses due to higher thermal gradients, as well as higher concentrations of reactive gases at the solid/liquid–gas interface. Due to thermal inertia, the thermal resolution of the two sub-steps improves with higher masses, as the second sub-step, which is linked to the decomposition of biuret in the melt, is shifted to higher temperatures. The overall mass loss during the first major decomposition range drops, because the concentration of evolved gases in the relative confinement of the crucible at the solid/liquid–gas interface increases with increasing sample mass, yielding a higher amount of non-volatile compounds as a result of a higher reaction rate. These trends for both temperatures and mass losses basically also hold true for the second major decomposition range. The third decomposition range is again consistently stepwise shifted to higher temperatures and mass losses, reflecting the sublimation of higher amounts of cyanuric acid formed during the previous decomposition steps. In accordance with the masses found for the pyrolysis residues at 550 °C, a fourth decomposition range is discernible for $m_0 = 3$–81 mg and gets more pronounced with increasing initial mass, confirming that the amount of aminated species formed at lower temperatures rises with the initial amount of sample employed.

Melon synthesis from urea

As our extensive TGA studies revealed, the reason for the apparent contradiction between ex situ and TGA methods, which clearly found condensed, aminated species during urea and biuret decomposition, and our own in situ TP-XRD and TP-DRIFTS measurements, which failed to, was based on different reaction conditions: the experimental setup during both DRIFTS (small amounts of sample diluted by KBr) and TP-XRD (flat-plate Bragg–Brentano diffractometer) does not allow for samples that are sufficiently thick to have a surface area to volume ratio small enough for evolved gases to react within the sample instead of being flushed away from the solid/liquid–gas interface by flushing gas streams. Moreover, the results of our TGA experiments suggested that a relatively closed crucible geometry, high heating rates and large sample masses were crucial pyrolysis parameters for successful melon syntheses; therefore, we decided to verify these assumptions by several syntheses on the gram scale with standard solid-state laboratory crucible shapes and sizes (one in the shape of a truncated cone with a volume of about 30 mL and three that were cylindrical with volumes of 60, 20 and 5 mL, as depicted from left to right, respectively, in Figure 5 d). The experiments yielded a highly porous powder, showing typical bluish luminescence under irradiation in the UV region (365 nm),[19,20] as well as a light-yellow body colour, sometimes with brownish discolourations on sample parts close to the crucible wall. A typical synthesis also leaves similar brownish stains on the upper part of the inner wall of the crucible employed. All products have been characterised through powder XRD and FTIR spectroscopy, yielding basically identical diffractograms and spectra (Figures S6 and S7 in the Supporting Information), in good agreement with those reported in the literature.[13] Because the FTIR spectra exhibit intense bands in the region around 3000 cm^{-1}, we attribute the synthesised samples to being closer to melon within the continuum of compounds, between the idealised chemical formulae of melon ($[C_6N_7(NH_2)(NH)]_n$) and g-C_3N_4, as found for many other carbon nitride species reported so far.[24,25]

The yields for each crucible geometry were reproducible within an accuracy of 0.1 % and are summarised in Table 4. Because it is widespread throughout scientific literature, the yields have been calculated with regard to the hypothetical chemical formula C_3N_4 for the sake of comparability, although it should be noted that true compositions are much more likely to be somewhere in the continuum between that of C_3N_4 (carbon nitride) and $H_3C_6N_9$ (melon), depending on the degree of condensation.[24,25] With increasing educt amounts and crucible volumes within the series of cylindrical crucibles, typical yields increasing from 1.6 to 4.4 % are expected from surface area to volume considerations. Changing the crucible to the shape of a truncated cone, but with a smaller volume further raises the yield, probably because these crucibles can carry a higher load per volume compared with that of their cylindrical equivalents due to the self-compacting effect of the conical shape for a poured random packing,[71,72] and thus, creating a higher concentration of evolved reactive gases during pyrolysis within the crucible. During these syntheses, we serendipitously encountered that reuse of the crucible in a second synthetic procedure, after carefully unloading and mechanically cleaning it with a glass rod, further darkened its stained inner walls and increased the obtained yields. Each further synthetic cycle enhanced both effects, as shown in Table 4, until, after about five cycles, a saturation of yield increase set in and the whole inner wall of the crucible was darkened from top to bottom. Through this process, the obtained yields could be more than doubled, rising from 4.9 to 11.1 %. Heating the empty crucible to 1200 °C in air completely restores the original colour of the crucible wall and resets the yield during the next melon synthesis conducted in it. To study the nature of these discolourations, a piece of aluminium foil was tucked between the crucible and its lid during synthesis, leading to similar brownish stains on it, which were subsequently characterised through X-ray photoelectron spectroscopy (XPS) on several positions with varying colour intensity (Figures S8 and S9 in the Supporting Information). As the spectra suggest, the brownish deposits are most probably graphitic carbon with small amounts of nitridation. The catalytic activity of carbon or melon itself on possible amination or condensation reactions was ruled out by adding active carbon or pre-synthesised melon to the employed urea, which had no significant impact on the obtained yields. Because Al_2O_3 is known to catalyse the reaction of urea to isocyanic acid and ammonia quite well,[6] we attribute the rising yields with more synthetic cycles to the increasing carbon coating of the crucible walls and the resulting reduced accessibility of catalytic sites on Al_2O_3. We further studied the influence of a few selected crucible materials (platinum or monel, which both completely suppressed the formation of melon, possibly also due to catalytic activity), but refrained from employing pure graphite crucibles because these show severe degradation under the reaction conditions.[73]

Table 4. Parameters of the experimental setup (crucible shape, volume and employed educt mass, respectively number of heating cycles a crucible has been employed for) and typical yields of the solid state syntheses from urea, under the assumption that the obtained product has the chemical formula C_3N_4.

Shape	Volume [mL]	Mass [g]	Yield [%]	No. cycles	Yield [%]
cylinder	5	4.5	1.6	1	4.9
cylinder	20	18	4.1	2	7.7
cylinder	60	49	4.4	3	8.9
tr. cone	30	29	4.9	4	11.1

Conclusion

We elucidated the crystal structure of water-free biuret through single-crystal XRD and characterised biuret at room temperature by means of powder XRD and FTIR spectroscopy. Based on these findings, we were able to perform and interpret TP-XRD and DRIFTS experiments to investigate in situ the thermal decomposition reaction of biuret, a crucial reaction intermediate during urea pyrolysis. By directly detecting the occurrence of a co-crystalline biuret–cyanuric acid phase during

decomposition, we could, for the first time, explain the well-known two-step degradation reaction from biuret to cyanuric acid. Because our measurements did not reveal any aminated decomposition products of biuret, although such products have been found by a variety of ex situ methods throughout the literature, we performed extensive TGA studies on biuret by varying crucible shape, heating rate, initial sample mass and flushing gas flow. Within these experiments, we discerned a massive impact of these parameters on the thermograms, corroborating that decomposition involved reactions on the solid/liquid–gas interface that were sensitive to the surface area to volume ratio of the studied samples. Deducing that high heating rates, large sample masses and closed crucible geometries were paramount for the formation of aminated decomposition products, we studied the synthesis of melon from urea on a gram scale. Our synthetic experiments with different alumina crucible sizes and shapes further emphasised our findings. Furthermore, we serendipitously observed the gradual coating of the inner walls of crucibles with slightly nitridised graphite (as suggested by XPS measurements) with each reuse of a crucible, together with an increase in yield of melon up to 11%. We attributed the latter to the diminished accessibility of catalytic sites on the surface of alumina, reducing the direct formation and subsequent loss of isocyanic acid and promoting the formation of condensed pyrolysis products. Although urea is, in terms of yield, still far inferior to, for example, melamine (up to 60%)[74] for melon synthesis, it should be noted that it is considerably cheaper and synthesis also provides still many possibilities for improvement. In particular, the use of fluidised bed reactors, such as those already employed for the synthesis of melamine from urea,[75] might be a promising technique for further yield optimisation and upscaling.

Experimental Section

Reagents

Biuret (97%, ACROS Organics) was recrystallised once from ethanol (96%, VWR chemicals). Single-crystal growth of biuret was achieved through slow evaporation from a saturated solution in ethanol at room temperature. Urea (p.a., Merck) was dried prior to use in a compartment drier at 80 °C for 24 h.

Single-crystal XRD

Suitable single crystals were picked under a polarising light microscope. Single-crystal XRD data of biuret were collected at a Bruker D8 Venture diffractometer by using $Mo_{K\alpha}$ radiation ($\lambda = 0.71073$ Å) from an Incoatec microfocus source and a Photon II CMOS detector. Absorption correction was performed through the multi-scan method with the SADABS program[76] within the APEX 3 suite.[77] Atomic positions of all atoms, apart from hydrogen atoms, were found by direct methods with SHELXS[78] and refined with anisotropic displacement parameters by full-matrix least-squares refinement against F^2 with SHELXL.[79] Hydrogen positions were determined by using a riding model and fixing the N–H distance to 0.95 Å with a standard deviation of 0.01.

Deposition Number 1986183 contains the supplementary crystallographic data for this paper. These data are provided free of charge by the joint Cambridge Crystallographic Data Centre and Fachinformationszentrum Karlsruhe Access Structures service www.ccdc.cam.ac.uk/structures.

Powder XRD

Room-temperature powder XRD patterns were recorded on a Seifert 3003 TT diffractometer in Bragg–Brentano geometry by using $Cu_{K\alpha}$ radiation, a GE METEOR 1D line detector and a nickel filter to suppress Kβ radiation (X-ray tube operated at 40 kV and 40 mA, scan range: 5–80°, increment: 0.02°, scans per data point: 40, integration time: 200 s/°). TP-XRD patterns were recorded on an Empyrean (PANalytical) diffractometer by using $Cu_{K\alpha}$ radiation, a Bragg-Brentano^{HD} mirror, a PIXcel^{3D} 2×2 detector and an Anton Paar XRK 900 reactor chamber (X-ray tube operated at 40 kV and 40 mA, scan range: 5–80°, increment: 0.02° with one step per 0.4 s). Temperatures between 25 and 350 °C were adjusted by heating at 0.5 °C s^{-1} and maintaining the same temperature for 10 min before starting each scan.

FTIR spectroscopy

Room-temperature IR spectra were recorded as ATR spectra with a Bruker EQUINOX 55 FTIR spectrometer, by using a platinum ATR device (scan range: 400–4000 cm^{-1}, resolution: 4 cm^{-1}, 32 scans per sample). TP IR spectra were recorded as DRIFTS spectra on the same spectrometer, by using a Praying Mantis™ high-temperature reaction chamber (Harrick Scientific) with KBr as a reference (scan range: 400–4000 cm^{-1}, resolution: 4 cm^{-1}, 32 scans per sample). Temperatures between 25 and 320 °C were adjusted by heating at 1 °C min^{-1} and maintaining the same temperature for 5 min before starting each scan.

TGA

TGA was performed with a NETZSCH STA 409 PC Luxx thermobalance under a nitrogen atmosphere (flow: 10–150 mL min^{-1}) in three different types of alumina crucibles (plate-like, cylindrical, and cylindrical with lid) at heating rates of 0.3–50 K min^{-1}) and sample masses between 1 and 81 mg.

Melon synthesis

In a typical synthesis, melon was prepared by filling crucibles of varying sizes and shapes (one in the shape of a truncated cone with a volume of about 30 mL and three cylindrical with volumes of 60, 20 and 5 mL) loosely with urea to the very top, sealing them with an alumina lid, and putting them into a chamber furnace preheated to 550 °C. The furnace was kept at that temperature for 2 h, then turned off and allowed to cool naturally to room temperature. Unloading of the crucibles was performed with a silica glass rod to avoid deposits of metal from a spatula onto the crucible walls, in case crucibles were reused after melon synthesis without further cleaning. In all other cases, crucibles were cleaned mechanically with a spatula, then boiled in aqua regia for 6 h followed by boiling in demineralised water for another 6 h, soaking in an *i*PrOH/KOH bath for 16 h, thorough flushing under demineralised water, and finally heating to 1200 °C in a chamber furnace in air.

XPS

XPS was performed with an Omicron XM 1000 monochromatised X-ray source with $Al_{K\alpha}$ radiation (1486.7 eV) and an Omicron EA125 hemispherical electron analyser. Survey scans were measured with a pass energy of 50 eV. A Shirley background was used for back-

ground subtraction. Chemical composition was determined by analysis of the XPS peak areas, which were corrected by the element- and orbital-specific sensitivity factors. The sum of the peak areas was normalised to 100%.

Acknowledgements

We thank Dr. Matthias Bauer for measuring the XPS spectra, Dipl.-Ing. Andreas Kalytta-Mewes for measuring the TP-XRD and Prof. Dr. rer. nat. habil. Micheal Ruck for fruitful discussions. Open access funding enabled and organized by Projekt DEAL.

Conflict of interest

The authors declare no conflict of interest.

Keywords: pyrolysis · reaction mechanisms · structure elucidation · urea · X-ray diffraction

[1] First description: a) J. B. V. Helmont, *Van Helmont's Works*. Translated into English by J. Chandler, L. Lloyd, **1664**; isolation: b) H. Boerhaave, *Elementa Chemiae*, Vol II, English translation by, T. Dallowe, 1727, Chapter Process XCVIII, pp. 317–318; composition: c) L. N. Vauquelin, A. F. de Fourcroy, *Annales du Muséum d Histoire Naturelle*, Vol. 11, 1808, Chapter Nouvelles expériences sur l urée, pp. 226–230; synthesis: d) C. Bosch, W. Meiser, *Process of Manufacturing Urea*, **1922**; quantitative analysis: e) J. K. Fawcett, J. E. Scott, *J. Clin. Path.* **1960**, *13*, 156–159; medical applications: f) M. Pan, G. Heinecke, S. Bernardo, C. Tsui, J. Levitt, *Dermatol. Online J.* **2013**, *19*, 20392.

[2] a) W. Prout, *Ann. Philos.* **1815**, *6*, 321–330; b) W. Prout, *Med. Chir. Trans.* **1817**, *MCT-8*, 521–544.

[3] a) F. Wöhler, *Ann. Phys. Chem.* **1828**, *88*, 253–256; b) E. Kinne-Saffran, R. K. H. Kinne, *Am. J. Nephrol.* **1999**, *19*, 290–294.

[4] a) H. A. Krebs, K. Z. Henseleit, *Physiol. Chem.* **1932**, *210*, 33; b) H. A. Krebs, *Trends Biochem. Sci.* **1982**, *7*, 76–78.

[5] P. M. Schaber, J. Colson, S. Higgins, D. Thielen, B. Anspach, J. Brauer, *Thermochim. Acta* **2004**, *424*, 131–142.

[6] A. M. Bernhard, D. Peitz, M. Elsener, A. Wokaun, O. Kröcher, *Appl. Catal. B* **2012**, *115–116*, 129–137.

[7] S. Sebelius, T. T. Le, L. J. Pettersson, H. Lind, *Chem. Eng. J.* **2013**, *231*, 220–226.

[8] F. Birkhold, U. Meingast, P. Wassermann, O. Deutschmann, *Appl. Catal. B* **2007**, *70*, 119–127.

[9] M. Eichelbaum, R. J. Farrauto, M. J. Castaldia, *Appl. Catal. B* **2010**, *97*, 90–97.

[10] a) M. Koebel, M. Elsener, M. Kleemann, *Catal. Today* **2000**, *59*, 335–345; b) G. Scheying, *Abgasbehandlungseinheit und Messvorrichtung zur Ermittlung einer Konzentration einer Harnstoff-Wasser-Lösung* **2003**; c) P. L. T. Gabrielsson, *Top. Catal.* **2004**, *28*, 177–184; d) S. D. Yim, S. J. Kim, J. H. Baik, I.-S. Nam, Y. S. Mok, J.-H. Lee, B. K. Cho, S. H. Oh, *Ind. Eng. Chem. Res.* **2004**, *43*, 4856–4863; e) V. Ebrahimian, A. Nicolle, C. Habchi, *AIChE J.* **2012**, *58*, 1998–2009.

[11] a) F. Dong, L. Wu, Y. Sun, M. Fu, Z. Wu, S. C. Lee, *J. Mater. Chem.* **2011**, *21*, 15171–15174; b) B. Chai, T. Peng, J. Mao, K. Lia, L. Zan, *Phys. Chem. Chem. Phys.* **2012**, *14*, 16745–16752; c) J. Liu, Y. Zhang, L. Lu, G. Wua, W. Chen, *Chem. Commun.* **2012**, *48*, 8826–8828; d) Y. Zhang, J. Liu, G. Wua, W. Chen, *Nanoscale* **2012**, *4*, 5300–5303; e) J. Mao, T. Peng, X. Zhang, K. Li, L. Ye, L. Zan, *Catal. Sci. Technol.* **2013**, *3*, 1253–1260; f) J. Xu, Y. Li, S. Peng, G. Lub, S. Li, *Phys. Chem. Chem. Phys.* **2013**, *15*, 7657–7665; g) W. Zhao, V. Fierro, N. Fernández-Huerta, M. Izquierdo, A. Celzard, *Int. J. Hydrogen Energy* **2013**, *38*, 10453–10460; h) Q. Su, J. Sun, J. Wang, Z. Yang, W. Cheng, S. Zhang, *Catal. Sci. Technol.* **2014**, *4*, 1556–1562; i) M. Zhang, J. Xu, R. Zong, Y. Zhu, *Appl. Catal. B* **2014**, *147*, 229–235; j) J. Liu, W. Li, L. Duan, X. Li, L. Ji, Z. Geng, K. Huang, L. Lu, L. Zhou, Z. Liu, W. Chen, L. Liu, S. Feng, Y. A. Zhang, *Nano Lett.* **2015**, *15*, 5137–5142; k) H.-B. Fang, Y. Luo, Y.-Z. Zheng, W. Ma, X. Tao, *Ind. Eng. Chem. Res.* **2016**, *55*, 4506–4514; l) A. Kharlamov, M. Bondarenko, G. Kharlamova, N. Gubareni, *Diam. Relat. Mater.* **2016**, *66*, 16–22; m) D. Nandi, S. Siwal, M. Choudhary, K. Mallick, *Appl. Catal. A* **2016**, *523*, 31–38; n) L. Zhang, H. Wang, W. Shen, Z. Qin, J. Wang, W. Fan, *J. Catal.* **2016**, *344*, 293–302; o) S. Cao, H. Chen, F. Jiang, X. Wang, *Appl. Catal. B* **2018**, *224*, 222–229; p) K. Dziubek, M. Citroni, S. Fanetti, A. B. Cairns, R. Bini, *J. Phys. Chem. C* **2017**, *121*, 19872–19879; q) Y. Zheng, Z. Zhang, C. Li, *J. Photochem. Photobiol. A* **2017**, *332*, 32–44; r) M. Ismael, Y. Wu, D. H. Taffa, P. Bottkea, M. Wark, *New J. Chem.* **2019**, *43*, 6909–6920.

[12] The crucial underlying amination process to melamine has been long known and exploited.[75]

[13] J. Liu, T. Zhang, Z. Wang, G. Dawson, W. Chen, *J. Mater. Chem.* **2011**, *21*, 14398–14401.

[14] Grünwald, J. D. Verbesserung der Reduktionsmitteldispersion und -verdunstung in SCR-Abgasanlagen. Ph.D. thesis, Technischen Universität München, **2007**.

[15] Y. Liao, P. D. Eggenschwiler, D. Rentsch, F. Curto, K. Boulouchos, *Appl. Energy* **2017**, *205*, 964–975.

[16] a) P. A. Brooks, Notice of Violation. Letter from the United States Environmental Protection Agency to Volkswagen AG, Audi AG and Volkswagen Group of America, Inc., **2015**; b) Ewing, J. Faster, Higher, Farther: *The Inside Story of the Volkswagen Scandal*, W. W. Norton & Company, **2017**.

[17] a) A. Y. Liu, M. L. Cohen, *Science* **1989**, *245*, 841–842; b) M. L. Cohen, *Science* **1993**, *261*, 307–308; c) D. M. Teter, R. J. Hemley, *Science* **1996**, *271*, 53–55; d) G. S. Manyali, R. Warmbier, A. Quandt, J. E. Lowther, *Comput. Mater. Sci.* **2013**, *69*, 299–303.

[18] a) G. Algara-Siller, N. Severin, S. Y. Chong, T. Björkman, R. G. Palgrave, A. Laybourn, M. Antonietti, Y. Z. Khimyak, A. V. Krasheninnikov, J. P. Rabe, U. Kaiser, A. I. Cooper, A. Thomas, M. J. Bojdys, *Angew. Chem. Int. Ed.* **2014**, *53*, 7450–7455; *Angew. Chem.* **2014**, *126*, 7580–7585; b) T. S. Miller, A. d'Aleo, T. Suter, A. E. Aliev, A. Sella, P. F. McMillan, *Z. Anorg. Allg. Chem.* **2017**, *643*, 1572–1580; c) J. Safaei, N. A. Mohamed, M. F. M. Noh, M. F. Soh, N. A. Ludin, M. A. Ibrahim, W. N. R. W. Isahak, M. A. M. Teridi, *J. Mater. Chem. A* **2018**, *6*, 22346–22380.

[19] Y. Zhang, Q. Pan, G. Chai, M. Liang, G. Dong, Q. Zhang, J. Qiu, *Sci. Rep.* **2013**, *3*, 1973.

[20] Z. Jiang, X. Zhang, J. Wang, L. Chen, H.-S. Chen, P. Yang, *Chem. Commun.* **2018**, *54*, 13519–13522.

[21] a) F. Goettmann, A. Fischer, M. Antonietti, A. Thomas, *Angew. Chem. Int. Ed.* **2006**, *45*, 4467–4471; *Angew. Chem.* **2006**, *118*, 4579–4583; b) N. D. Shcherban, *Theor. Exp. Chem.* **2016**, *52*, 265–284; c) I. Y. Kim, S. Kim, X. Jin, S. Premkumar, G. Chandra, N.-S. Lee, G. P. Mane, S.-J. Hwang, S. Umapathy, A. Vinu, *Angew. Chem. Int. Ed.* **2018**, *57*, 17135–17140; *Angew. Chem.* **2018**, *130*, 17381–17386; d) P. Zhou, X. Hou, Y. Chao, W. Yang, W. Zhang, Z. Mu, J. Lai, F. Lv, K. Yang, Y. Liu, J. Li, J. Ma, J. Luo, S. Guo, *Chem. Sci.* **2019**, *10*, 5898–5905; e) R. Shi, C. Tian, X. Zhu, C.-Y. Peng, B. Mei, L. He, X.-L. Du, Z. Jiang, Y. Chen, S. Dai, *Chem. Sci.* **2019**, *10*, 2585–2591.

[22] a) X. Wang, K. Maeda, A. Thomas, K. Takanabe, G. Xin, J. M. Carlsson, K. Domen, M. Antonietti, *Nat. Mater.* **2009**, *8*, 76–80; b) Y. Wang, X. Wang, M. Antonietti, *Angew. Chem. Int. Ed.* **2012**, *51*, 68–89; *Angew. Chem.* **2012**, *124*, 70–92; c) Y. Hou, F. Zuo, A. P. Dagg, J. Liu, P. Feng, *Adv. Mater.* **2014**, *26*, 5043–5049; d) C. A. Caputo, M. A. Gross, V. W. Lau, C. Cavazza, B. V. Lotsch, E. Reisner, *Angew. Chem.* **2014**, *126*, 11722–11726; e) K. Schwinghammer, M. B. Mesch, V. Duppel, C. Ziegler, J. Senker, B. V. Lotsch, *J. Am. Chem. Soc.* **2014**, *136*, 1730–1733; f) G. Liu, T. Wang, H. Zhang, X. Meng, D. Hao, K. Chang, P. Li, T. Kako, J. Ye, *Angew. Chem.* **2015**, *127*, 13765–13769; g) G. Zhang, Z.-A. Lan, L. Lin, S. Lin, X. Wang, *Chem. Sci.* **2016**, *7*, 3062–3066; h) Y. Guo, J. Li, Y. Yuan, L. Li, M. Zhang, C. Zhou, Z. Lin, *Angew. Chem. Int. Ed.* **2016**, *55*, 14693–14697; *Angew. Chem.* **2016**, *128*, 14913–14917; i) V. W. Lau, I. Moudrakovski, T. Botari, S. Weinberger, M. B. Mesch, V. Duppel, J. Senker, V. Blum, B. V. Lotsch, *Nat. Commun.* **2016**, *7*, 12165; j) S. Patnaik, S. Martha, S. Acharya, K. M. Parida, *Inorg. Chem. Front.* **2016**, *3*, 336–347; k) A. Naseri, M. Samadi, A. Pourjavadi, A. Z. Moshfegh, S. Ramakrishna, *J. Mater. Chem. A* **2017**, *5*, 23406–23433; l) V. W. Lau, V. W.-Z. Yu, F. Ehrat, T. Botari, I. Moudrakovski, T. Simon, V. Duppel, E. Medina, J. K. Stolarczyk, J. Feldmann, V. Blum, B. V. Lotsch, *Adv. Energy Mater.* **2017**, *7*, 1602251; m) G. Zhang, Z.-A. Lan, X. Wang, *Chem. Sci.* **2017**, *8*, 5261–5274; n) H. Wang, S. Jiang, S. Chen,

X. Zhang, W. Shao, X. Sun, Z. Zhao, Q. Zhang, Y. Luo, Y. Xie, *Chem. Sci.* **2017**, *8*, 4087 – 4092; o) M. Volokh, G. Peng, J. Barrio, M. Shalom, *Angew. Chem. Int. Ed.* **2019**, *58*, 6138; *Angew. Chem.* **2019**, *131*, 6138.

[23] a) C. Niu, Y. Z. Lu, C. M. Lieber, *Science* **1993**, *261*, 334 – 337; b) G. Demazeau, H.. Montigau, Tan-B##guy, M. Birot, J. Dunogues, *Rev. High Pressure Sci. Technol.* **1998**, *7*, 1345 – 1347; c) E. Kroke, M. Schwarz, E. Horath-Bordon, P. Kroll, B. Noll, A. D. Norman, *New J. Chem.* **2002**, *26*, 508 – 512; d) E. Kroke, M. Schwarz, *Coord. Chem. Rev.* **2004**, *248*, 493 – 532; e) E. Horvath-Bordon, R. Riedel, A. Zerr, P. F. McMillan, G. Auffermann, Y. Prots, W. Bronger, R. Kniep, P. Kroll, *Chem. Soc. Rev.* **2006**, *35*, 987 – 1014; f) E. Horvath-Bordon, R. Riedel, P. F. McMillan, P. Kroll, G. Miehe, P. A. van Aken, A. Zerr, P. Hoppe, O. Shebanova, I. McLaren, S. Lauterbach, E. Kroke, R. Boehler, *Angew. Chem. Int. Ed.* **2007**, *46*, 1476 – 1480; *Angew. Chem.* **2007**, *119*, 1498 – 1502.

[24] a) B. V. Lotsch, M. Döblinger, J. Sehnert, L. Seyfarth, J. Senker, O. Oeckler, W. Schnick, *Chem. Eur. J.* **2007**, *13*, 4969 – 4980; b) J. R. Holst, E. G. Gillan, *J. Am. Chem. Soc.* **2008**, *130*, 7373 – 7379.

[25] a) M. J. Bojdys, J.-O. Müller, M. Antonietti, A. Thomas, *Chem. Eur. J.* **2008**, *14*, 8177 – 8182; b) G. Goglio, D. Foy, G. Demazeau, *Mater. Sci. Eng. R* **2008**, *58*, 195 – 227; c) M. Döblinger, B. V. Lotsch, J. Wack, J. Thun, J. Senker, W. Schnick, *Chem. Commun.* **2009**, 1541 – 1543; d) J. Gracia, P. Kroll, *J. Mater. Chem.* **2009**, *19*, 3013 – 3019; e) A. V. Semencha, L. N. Blinov, *Glass Phys. Chem.* **2010**, *36*, 199 – 208; f) E. Wirnhier, M. Döblinger, D. Gunzelmann, J. Senker, B. V. Lotsch, W. Schnick, *Chem. Eur. J.* **2011**, *17*, 3213 – 3221; g) T. Tyborski, C. Merschjann, S. Orthmann, F. Yang, M.-C. Lux-Steiner, T. Schedel-Niedrig, *J. Phys. Condens. Matter* **2013**, *25*, 395402; h) A. Schwarzer, T. Saplinova, E. Kroke, *Coord. Chem. Rev.* **2013**, *257*, 2032 – 2062; i) F. Fina, S. K. Callear, G. M. Carins, J. T. S. Irvine, *Chem. Mater.* **2015**, *27*, 2612 – 2618; j) T. S. Miller, A. B. Jorge, T. M. Suter, A. Sella, F. Cora, P. F. McMillan, *Phys. Chem. Chem. Phys.* **2017**, *19*, 15613 – 15638; k) T. Botari, W. P. Huhn, V. W. Lau, B. V. Lotsch, V. Blum, *Chem. Mater.* **2017**, *29*, 4445 – 4453.

[26] H. Kinoshita, *IV. Rev. Phys. Chem. Jpn.* **1955**, *25*, 34 – 37.

[27] G. Ostrogovich, R. Bacaloglu II, *Rev. Roum. Chim.* **1965**, *10*, 1111 – 1128.

[28] L. Stradella, M. Argentero, *Thermochim. Acta* **1993**, *219*, 315 – 323.

[29] M. Koebel, M. Elsener, *J. Chromatogr. A* **1995**, *689*, 164 – 169.

[30] J. P. Chen, K. Isa, *J. Mass Spectrom. Soc. Jpn.* **1998**, *46*, 299 – 303.

[31] P. M. Schaber, J. Colson, S. Higgins, E. Dietz, D. Thielen, B. Anspach, J. Brauer, *Am. Lab.* **1999**, *31*, 13 – 21.

[32] O. Carp, *Rev. Roum. Chim.* **2001**, *46*, 735 – 740.

[33] H. L. Fang, H. F. M. DaCosta, *Appl. Catal. B* **2003**, *46*, 17 – 34.

[34] A. Lundström, B. Andersson, L. Olsson, *Chem. Eng. J.* **2009**, *150*, 544 – 550.

[35] M. Eichelbaum, A. B. Siemer, R. J. Farrauto, M. J. Castaldia, *Appl. Catal. B* **2010**, *97*, 98 – 110.

[36] W. Yang, Z. Chen, J. Zhou, Z. Huang, K. Cen, *Ind. Eng. Chem. Res.* **2011**, *50*, 7990 – 7997.

[37] J. M. Jones, A. N. Rollinson, *Thermochim. Acta* **2013**, *565*, 39 – 45.

[38] L. Sandoval Rangel, J. R. de la Rosa, C. J. L. Ortiz, M. J. Castaldi, *J. Anal. Appl. Pyrolysis* **2015**, *113*, 564 – 574.

[39] S. Tischer, M. Börnhorst, J. Amsler, G. Schoch, O. Deutschmann, *Phys. Chem. Chem. Phys.* **2019**, *21*, 16785 – 16797.

[40] D. Wang, N. Dong, S. Hui, Y. Niu, *Fuel* **2019**, *242*, 62 – 67.

[41] W. Brack, B. Heine, F. Birkhold, M. Kruse, G. Schoch, S. Tischer, O. Deutschmann, *Chem. Eng. Sci.* **2014**, *106*, 1 – 8.

[42] F. Rafa, *Arch. Appl. Sci. Res.* **2014**, *6*, 75 – 78.

[43] J. Liebig, *Ann. Phys.* **1835**, *110*, 570 – 613.

[44] J. Liebig, *Ann. Pharm.* **1834**, *10*, 1 – 47.

[45] F. Wöhler, *Ann. Phys.* **1829**, *91*, 619 – 630.

[46] H. Kohlmann, *Eur. J. Inorg. Chem.* **2019**, 4174 – 4180.

[47] a) The crystal structure of urea was the first acyclic molecular structure elucidated by means of XRD; see: H. Mark, K. Weissenberg, *Z. Phys.* **1923**, *42*, 255 – 256; b) the crystal structure of cyanuric acid was the first heterocycle elucidated by means of XRD; see: E. H. Wiebenga, N. F. Moerman, *Nature* **1938**, *141*, 122;[78] refined by the least-squares method.[67]

[48] A. M. Bernhard, I. Czekaj, M. Elsener, A. Wokaun, O. Kröcher, *J. Phys. Chem. A* **2011**, *115*, 2581 – 2589.

[49] a) G. H. Wiedemann, *J. Prakt. Chem.* **1847**, *42*, 255 – 256; b) G. H. Wiedemann, *Ann. Phys. Chem.* **1848**, *150*, 67 – 84; c) G. H. Wiedemann, *J. Prakt. Chem.* **1848**, *43*, 271 – 280; d) G. H. Wiedemann, *Ann. Chem. Pharm.* **1848**, *68*, 323 – 326.

[50] J. W. Knipe, G. F. G. Menary, *S. Afr. J. Chem.* **1958**, *11*, 37 – 41.

[51] E. W. Hughes, H. L. Yakel, H. C. Freeman, *Acta Crystallogr.* **1961**, *14*, 345 – 352.

[52] S. Haddad, P. S. Gentile, *Inorg. Chim. Acta* **1975**, *12*, 131 – 138.

[53] N. M. Stainton, K. D. M. Harris, R. A. Howie, *Chem. Commun.* **1991**, 1781 – 1784.

[54] M. M. Bishop, L. F. Lindoy, S. Mahadev, P. J. Turner, *Chem. Soc. Dalton Trans.* **2000**, 233 – 234.

[55] A. V. Kazakova, N. D. Kushch, A. N. Chekhlov, A. D. Dubrovskii, E. B. Yagubskii, K. V. Van, *Zh. Obshch. Khim.* **2009**, *79*, 9.

[56] M. Tutughamiarso, E. Egert, *Acta Crystallogr. Sect. B* **2012**, *68*, 444 – 452.

[57] I. Matulková, J. Mathauserová, I. Cisarová, I. Nemec, J. Fábry, *Z. Kristallogr. Cryst. Mater.* **2016**, *231*, 291 – 300.

[58] R. D. Shannon, *Acta Crystallogr. Sect. A* **1976**, *32*, 751 – 767.

[59] P. Gross, H. Höppe, *Z. Anorg. Allg. Chem.* **2017**, *643*, 1692 – 1703.

[60] P. Gross, H. Höppe, *Chem. Mater.* **2019**, *31*, 8052 – 8061.

[61] P. Gross, H. Höppe, *Z. Anorg. Allg. Chem.* **2019**, *645*, 257 – 266.

[62] L. R. Falvello, I. Pascual, M. Tomás, E. P. Urriolabeitia, *J. Am. Chem. Soc.* **1997**, *119*, 11894 – 11902.

[63] B. Jürgens, E. Irran, J. Senker, P. Kroll, H. Müller, W. Schnick, *J. Am. Chem. Soc.* **2003**, *125*, 10288 – 10300.

[64] A. Sattler, W. Schnick, *Z. Anorg. Allg. Chem.* **2006**, *632*, 238 – 242.

[65] B. V. Lotsch, W. Schnick, *Chem. Eur. J.* **2007**, *13*, 4956 – 4968.

[66] E. Wirnhier, M. B. Mesch, J. Senker, W. Schnick, *Chem. Eur. J.* **2013**, *19*, 2041 – 2049.

[67] E. W. Hughes, *J. Am. Chem. Soc.* **1941**, *63*, 1737 – 1752..

[68] B. V. Lotsch, From Molecular Building Blocks to Condensed Carbon Nitride Networks: Structure and Reactivity. Ph.D. thesis, Ludwig-Maximilians-Universität München, **2006**.

[69] J. Liebig, F. Wöhler, *Ann. Phys. Chem.* **1830**, *96*, 369 – 400.

[70] W. Kern, H. Paul, W. Mehren, *Makromol. Chem.* **1954**, *14*, 146 – 155.

[71] F. A. L. Dullien, *Porous Media: Fluid Transport and Pore Structure*, Academic Press, **1991**.

[72] M. Berhanu, A. Kudrolli, *Phys. Rev. Lett.* **2010**, *105*, 098002.

[73] L. Xiaowei, R. Jean-Charles, Y. Suyuan, *Nucl. Eng. Des.* **2004**, *227*, 273 – 280.

[74] Y. Yuan, L. Zhang, J. Xing, M. I. B. Utama, X. Lu, K. Du, Y. Li, X. Hu, S. Wang, A. Genç, R. Dunin-Borkowski, J. Arbiold, Q. Xiong, *Nanoscale* **2015**, *7*, 12343 – 12350.

[75] A. Schmidt, *Chem. Ing. Tech.* **1966**, *38*, 1140 – 1144.

[76] Bruker, SADABS. **2001**; Bruker AXS Inc.; Madison, Wisconsin, USA.

[77] Bruker, APEX2. **2012**; Bruker AXS Inc.; Madison, Wisconsin, USA.

[78] G. M. Sheldrick, *Acta Crystallogr. Sect. A* **2008**, *64*, 112 – 122.

[79] G. M. Sheldrick, *Acta Crystallogr. Sect. C* **2015**, *71*, 3 – 8.

Manuscript received: March 20, 2020
Revised manuscript received: June 6, 2020
Accepted manuscript online: June 23, 2020
Version of record online: October 7, 2020